DISCOID AND ASYMMETRICAL GYROLESS MICRO-SATELLITE OFF-MODULATION ATTITUDE CONTROL WITH KALMAN FILTER

Ho-Nien Shou

Department of Aviation & Communication Electronics, Air Force Institute of Technology, Kaohsiung City, Taiwan, R.O.C., honien.shou@mail.afats.khc.edu.tw

DISCOID AND ASYMMETRICAL GYROLESS MICRO-SATELLITE OFF-MODULATION ATTITUDE CONTROL WITH KALMAN FILTER

Acknowledgements

DISCOID AND ASYMMETRICAL GYROLESS MICRO-SATELLITE OFF-MODULATION ATTITUDE CONTROL WITH KALMAN FILTER

Ho-Nien Shou

ABSTRACT

The gyroless attitude control method and kalman algorithm procedures presented in this paper are applicable to asymmetrical microsatellites of any shape with large mass variation and without angular rate sensors. The attitude sensors include a three-axis magnetometer, a horizon sensor, and a coarse sun sensor (CSS), which together serve as an analytic platform and help in ensuring the stability of attitude controls.

The attitude control problem of microsatellites has become a focal point because microsatellite fabrication processes are short, costless, and can be flexibly used for various purposes. The center of mass of the microsatellite can be offset because of fuel consumption during propulsion, irrespective of the existence of interference from the external orbital environment, such as gravity gradient torque and solar radiation torque. For a microsatellite with a discoid and asymmetrical shape, attitude control is difficult. One of the solutions to overcome the difficulty is to design a robust controller that assists the attitude pointing of the satellite to satisfy requirements in the presence of internal parameter perturbations and external disturbances. The robust nonlinear state feedback used in the design of the propulsion mode attitude control for FORMOSAT-3 was applied in this study, and the feasibility of the controller was cross-validated through time and frequency domain stability analyses.

The time-domain performance indexes (e.g., rise time, maximum overshoot, and stabilization time) of the designed state feedback gain were consistent with a robust stability margin of the stable performance index in the frequency domain. Furthermore, to reduce the weight and manufacturing cost of the satellite, an extended Kalman filter algorithm was used to

obtain the gyroless satellite attitude rate. Other sensors, such as the CSS and earth horizon sensor were adopted to help sense satellite attitude controls.

I. INTRODUCTION

The discoid and asymmetrical satellite propulsion mode attitude control with large mass change developed a real-time dynamic simulation system and the technology. A processor used for attitude control was used to test the processor in the loop to determine the suitability of the processor for a microsatellite system. The establishment of an analytic method and control technique is necessary for attitude stabilization of microsatellites of all shapes and with large mass variation.

The basic attitude sensors of a satellite include a combination of attitude and rate sensors. The attitude sensors include a coarse sun sensor (CSS), a horizon sensor, a magnetometer, and a star tracker. The attitude rate sensor used is the gyro. The gyro is expensive, and it is unreliable because of reference point drift and is a major source of measurement error. It is more likely to be faulty compared with attitude sensors. With the increasing use of satellite technology, satellite construction cost must be reduced. Furthermore, with advances in software and algorithmic techniques, software-based processing of attitude data for obtaining attitude rate information has become reliable. Thus, the gyro has been removed by engineers. Consequently, gyroless design has become the trend in recent research [7, 12]. The following activities were performed in the present study:

1) An extended Kalman filter (EKF) algorithm was used for gyroless satellite attitude determination. The EKF structure is simple, and the hardware configuration requirement is not strict. It is especially applicable to low-cost microsatellites [3, 10].

2) A robust controller satisfying the interference condition requirement was designed for performing attitude pointing control when changes occur in the center of mass [13].

3) The sun azimuth vector is the third available reference vector that is used most in attitude determination methods. A sun sensor determines the orientation of the sun in a

sensitive coordinate system according to the change in the solar radiation intensity following a change in the satellite attitude [11].

4) In some cases, some sensors fail or the measurement accuracy decreases considerably; therefore, the attitude information cannot be obtained completely. Consequently, the single-point deterministic attitude computation is no longer possible. It is then necessary to introduce filtering in the attitude determination loop to enhance the robustness of the system. This study used a EKF algorithm for six-dimensional attitude estimation based on two/three observation vectors without using an angular rate sensor.

The remainder of this paper is organized as follows: Section II describes the concept of satellite attitude and Section III presents a microsatellite attitude control model. The robust nonlinear state feedback is explained in Section IV, Section V introduces extended Kalman filtering and a EKF algorithm, Section VI describes the measurement reference model, Section VII discusses an analysis of the attitude determination subsystem, and the last section is the conclusion.

II. DESCRIPTION OF SATELLITE ATTITUDE

1. Coordinate System and Orbit Parameters

The coordinate systems and orbit parameters used in this study are as follows.

1) Geographic coordinate system: The origin of the geographic coordinate system is the location of the satellite on the earth's surface; the x axis points to the east, the y axis points to the north, and the z axis points to the earth's center (i.e., the local vertical direction). The x, y, and z axes form a right-handed coordinate system. Quantities related to this coordinate system are marked with subscript g.

2) Local vertical local horizontal coordinate system: The origin is the satellite center of mass. The x axis points in the satellite flight direction, the y axis points in the negative direction of the normal to the orbital plane, and the z axis, which is defined according to the right-hand rule, points to the earth's center. The orbit system is an important reference for attitude control. Quantities related to this coordinate system are marked with right subscript o.

3) Body coordinates: The origin is located at the satellite center of mass. The three coordinate axes coincide with the principal axis of inertia of the satellite body. The satellite body system and the orbit system are identical when the three-axis attitude of the satellite is stable. Quantities related to the satellite body system are marked with right subscript b.

4) Earth-centered inertial (ECI) coordinate system: The origin is located at the earth's center of mass, the x axis points to the vernal equinox; the z axis points to the north pole along the earth's spin axis, and the y axis is defined by the

right-hand rule. Quantities related to this coordinate system are marked with right superscript i.

5) Earth-centered Earth-fixed (ECEF) coordinate system: The origin is located at the earth's center, the x axis points to the Greenwich zero meridian in the equatorial plane, the z axis points to the north pole along the earth's spin axis, and the y axis is defined by the right-hand rule. Quantities related to this coordinate system are marked with right subscript e.

For the motion of a satellite in a circumterrestrial orbit, the ECI coordinate system is used to study the motion, and the orbit system is considered as the reference coordinate system for describing the satellite, with the three axes stably pointing to the earth. Coordinate systems are switched as required. For example, the geomagnetic field and sun vector models in this study were switched to the orbit system.

2. Description of Quaternion Attitude

The quaternion-based satellite attitude consists of one scalar part and three vector parts, defined as [12]

$$\boldsymbol{q} = q_0 + q_1 i + q_2 j + q_3 k = \begin{bmatrix} q_0 & q^T \end{bmatrix} \tag{1}$$

where q_0 is the quaternion scalar part and q is the vector part. The four parameters meet the following constraint condition:

$$\sum_{i=0}^{3} q_i^2 = 1 \tag{2}$$

Therefore, only three of the four quaternion variables are independent. According to the definition of Euler's rotation and quaternion, the conversion of the attitude between the orbit system and the satellite body system is described by a quaternion. The attitude rotation matrix for the conversion from the orbit system to the satellite body system is

$$C_o^b = \begin{bmatrix} 1-2\left(q_2^2+q_3^2\right) & 2\left(q_1q_2+q_0q_3\right) & 2\left(q_1q_3-q_0q_2\right) \\ 2\left(q_1q_2-q_0q_3\right) & 1-2\left(q_1^2+q_3^2\right) & 2\left(q_2q_3+q_0q_1\right) \\ 2\left(q_1q_3+q_0q_2\right) & 2\left(q_2q_3-q_0q_1\right) & 1-2\left(q_1^2+q_2^2\right) \end{bmatrix} \tag{3}$$

The quaternion attitude matrix consists of a quadratic term involving the quaternion $\boldsymbol{q}$; therefore, the quaternion $-\boldsymbol{q} = \begin{bmatrix} -q_0 & -q^T \end{bmatrix}^T$ can be used to obtain the attitude matrix shown in Eq. (3). The nonuniqueness of the quaternion is consistent with the nonuniqueness of the Euler axis/angle. For instance, if the Euler rotation angles are 0 and 2π, the corresponding quaternions are $\begin{bmatrix} 1 & 0 & 0 & 0 \end{bmatrix}^T$ and $\begin{bmatrix} -1 & 0 & 0 & 0 \end{bmatrix}^T$, respectively. However, both quaternions physically represent the same attitude and the same rotation. This study used a positive value of the quaternion for calculations. If Eq. (3) is written in vector form, then

$$C_o^b = I_3 - q_0 q^\times + \left(q^\times\right)^2 \tag{4}$$

or

$$C_o^b = \left(q_0^2 - q^T q\right) I_3 + 2qq^T - 2q_0 q^\times \tag{5}$$

where $q^\times$ represents the skew symmetric matrix

$$q^\times = \begin{bmatrix} 0 & -q_3 & q_2 \\ q_3 & 0 & -q_1 \\ -q_2 & q_1 & 0 \end{bmatrix} \tag{6}$$

3. Properties of Attitude Rotation Matrix

The attitude rotation matrix C_o^b in Eq. (3) can be expressed as

$$C_o^b = \begin{bmatrix} c_1 & c_2 & c_3 \end{bmatrix} \tag{7}$$

where $c_i = \begin{bmatrix} c_{1i} & c_{2i} & c_{3i} \end{bmatrix}^T$, $i = 1, 2, 3$, represents the direct cosine vector. C_o^b is an orthogonal matrix, and its properties are presented below:

$$C_o^b = \left(C_b^o\right)^{-1} = \left(C_b^o\right)^T$$

$$c_1 \times c_2 = c_3, c_2 \times c_3 = c_1, c_3 \times c_1 = c_2, \left(c_{1i}\right)^2 + \left(c_{2i}\right)^2 + \left(c_{3i}\right)^2 = 1$$

and

$$\left(c_{j1}\right)^2 + \left(c_{j2}\right)^2 + \left(c_{j3}\right)^2 = 1 \tag{8}$$

The projection of the angular rate in the satellite body system to the orbit system is defined as ω_o^b. The following relationship can be deduced for the attitude rotation matrix C_o^b:

$$\dot{C}_o^b = -C_o^b \left(\omega_o^b\right)^\times, \dot{c}_i = c_i \times \omega_o^b = \left(c_i\right)^\times \omega_o^b \tag{9}$$

III. ATTITUDE CONTROL MODEL OF MICROSATELLITE

1. Microsatellite Thrust-Torque Deduction

Figs. 1(a) and (b) show a discoid and asymmetrical microsatellite. The four thrust nozzles of the microsatellite are in the xz plane at inclination α, and the nozzles point to the y-direction, laid in square at intervals of d. The fuel tank is in the xz plane l of the nozzle and is at distance $-y$ from the centroid position of the microsatellite. The body coordinates of the microsatellite FORMOSAT-3 are shown in Fig. 1(c); $\Delta\alpha$,
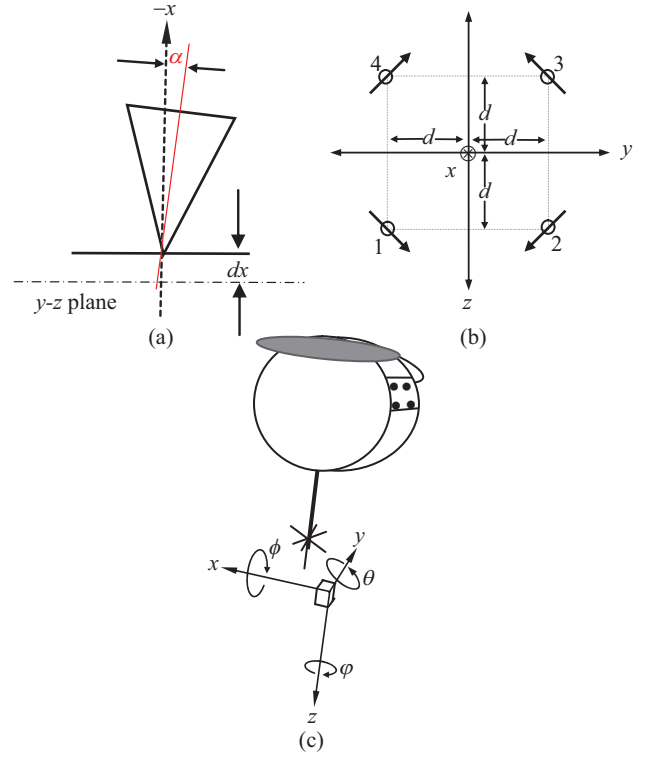
Fig. 1. Geometric graph of a micro-satellite.

Δd, and Δl represent the uncertainties in nozzle inclination, relative distance between nozzles and the fuel tank, and centroid position offset, respectively. The nozzle thrust direction and the force-arm-generated torque are determined as follows:

$$\vec{F}_1 = -f_s \vec{e}_x + f_c \vec{e}_y + f_s \vec{e}_z, \vec{F}_2 = f_s \vec{e}_x + f_c \vec{e}_y + f_s \vec{e}_z$$

$$\vec{F}_3 = f_s \vec{e}_x + f_c \vec{e}_y - f_s \vec{e}_z, \vec{F}_4 = -f_s \vec{e}_x + f_c \vec{e}_y - f_s \vec{e}_z$$

$$f_s = \frac{1}{\sqrt{2}} \sin(\alpha + \Delta\alpha), \ f_c = \cos(\alpha + \Delta\alpha) \tag{10}$$

$$\vec{r}_1 = \left(d_x + \Delta d_x\right)\vec{e}_x - \left(l + \Delta l\right)\vec{e}_y + \left(d_y + \Delta d_y\right)\vec{e}_z$$

$$\vec{r}_2 = -\left(d_x + \Delta d_x\right)\vec{e}_x - \left(l + \Delta l\right)\vec{e}_y + \left(d_z + \Delta d_z\right)\vec{e}_z$$

$$\vec{r}_3 = -\left(d_x + \Delta d_x\right)\vec{e}_x - \left(l + \Delta l\right)\vec{e}_y - \left(d_z + \Delta d_z\right)\vec{e}_z$$

$$\vec{r}_4 = \left(d_x + \Delta d_x\right)\vec{e}_x - \left(l + \Delta l\right)\vec{e}_y - \left(d_z + \Delta d_z\right)\vec{e}_z \tag{11}$$

Here,

$$\left|\frac{\Delta d_x}{d_x}\right| \le 0.2, \left|\frac{\Delta d_z}{d_z}\right| \le 0.2, \left|\frac{\Delta l}{l}\right| \le 0.2, \text{ and } \left|\frac{\Delta\alpha}{\alpha}\right| \le 0.2. \tag{12}$$

If $\alpha + \Delta\alpha$ is very small, the torque τ_u can be obtained as follows:

$$\begin{bmatrix} \tau_{u_x} \\ \tau_{u_y} \\ \tau_{u_z} \end{bmatrix} = \begin{bmatrix} -\beta_{1\Delta} & -\beta_{1\Delta} & \beta_{1\Delta} & \beta_{1\Delta} \\ -\beta_{2\Delta} & \beta_{2\Delta} & -\beta_{2\Delta} & -\beta_{2\Delta} \\ \beta_{3\Delta} & -\beta_{3\Delta} & -\beta_{3\Delta} & \beta_{3\Delta} \end{bmatrix} \begin{bmatrix} u_1 \\ u_2 \\ u_3 \\ u_4 \end{bmatrix} = \boldsymbol{\beta} u \quad (13)$$

where

$$\beta_{i\Delta} = \beta_i + \Delta\beta_i, i = 1, 2, 3$$

$$\beta_1 = d + \frac{\alpha l}{\sqrt{2}}, \beta_2 = \sqrt{2}\alpha d, \beta_3 = d - \frac{\alpha l}{\sqrt{2}}$$

$$\Delta\beta_1 = \Delta d + \frac{1}{\sqrt{2}}\left(\alpha\Delta l + l\Delta\alpha + \Delta\alpha\Delta l\right)$$

$$\Delta\beta_2 = \sqrt{2}\left(\alpha\Delta l + l\Delta\alpha + \Delta\alpha\Delta l\right)$$

$$\Delta\beta_3 = \Delta d - \frac{1}{\sqrt{2}}\left(\alpha\Delta l + l\Delta\alpha + \Delta\alpha\Delta l\right) \quad (14)$$

2. On/Off-Modulated Thrust Control

From the controller commands transform into pulse width modulation, the thrust control process is as follows [9]:

1) The thruster generates commands $\boldsymbol{u}$.
2) Convert $\boldsymbol{u}$(n) from variable thrusts for a fixed total sample period to fixed thrusts for variable times: t_on = (sample time/thrust magnitude) $\times \boldsymbol{u}$.
3) Limit on-times to $\pm$ half the sample period.
4) Compute a bias term and add the bias to all on-times such that at least one thruster is on for the complete sample period.

According to the pulse width modulation duty rule, the sample period can be divided into two types of modulation: off and on modulation. In this processing, off-modulation is adopted. A block diagram of pulse width modulation used for microsatellite attitude control is shown in Fig. 2. At least one thruster is operating during off modulation, and at least one thruster is turned off during on modulation.

IV. ROBUST NONLINEAR STATE FEEDBACK

The kinematic equation of a microsatellite is written as

$$\dot{\boldsymbol{q}} = \frac{1}{2}\begin{bmatrix} -\boldsymbol{\omega}^{\times} & \boldsymbol{\omega} \\ -\boldsymbol{\omega}^T & 0 \end{bmatrix}\begin{bmatrix} \mathrm{q} \\ q_0 \end{bmatrix} = \frac{1}{2}\begin{bmatrix} \mathrm{q}^{\times} + q_0 I \\ -\mathrm{q}^T \end{bmatrix}\boldsymbol{\omega}$$

$$= \frac{1}{2}Q(\boldsymbol{q})\boldsymbol{\omega} \quad (15)$$

where
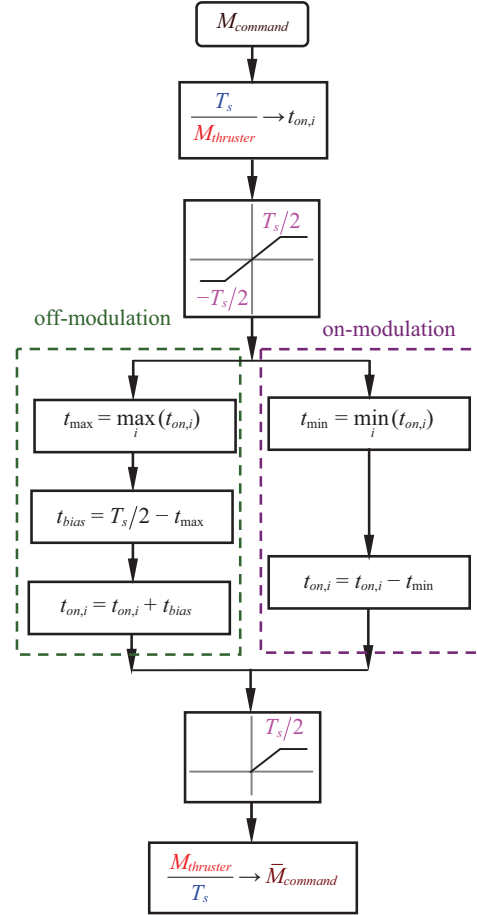
Fig. 2. Block diagram of on/off-modulated thrust control.

$$Q(\boldsymbol{q}) \triangleq \frac{1}{2}\begin{bmatrix} \mathrm{q}^{\times} + q_0 I \\ -\mathrm{q}^T \end{bmatrix}$$

In attitude control design, the system should be stable and the excursions of the angular rate and control input should be minimized. This prompts the use of the following penalty function, which is to be minimized:

$$z = \begin{bmatrix} \sqrt{\rho_1 \boldsymbol{\omega}^T J_{\Delta} \boldsymbol{\omega} + \rho_2 \eta^2\left(q_0\right)} \\ \rho_3 \boldsymbol{u} \end{bmatrix}$$

where ρ_1, ρ_2, and ρ_3 are weighting coefficients introduced for controlling the trade-off between performance and control effort. The function $\eta(q_0)$ is defined as $\eta(q_0) = 2\cos^{-1}\left|q_0\right|$.

The attitude control problem can then be formulated as

$$\dot{\boldsymbol{x}} = \left(f(\boldsymbol{x}) + \Delta f(\boldsymbol{x})\right) + \left(g_1(\boldsymbol{x}) + \Delta g_1(\boldsymbol{x})\right)\boldsymbol{w}$$

$$+ \left(g_2(\boldsymbol{x}) + \Delta g_2(\boldsymbol{x})\right)\boldsymbol{u} \quad (16)$$

$$z = \begin{bmatrix} h(\pmb{x}) \\ \pmb{u} \end{bmatrix} = h_1(\pmb{x})$$

where $\pmb{x} = \begin{bmatrix} \pmb{\omega}^T & \mathrm{q}^T & q_0 \end{bmatrix}^T$ is the state $\pmb{x}$, and $\pmb{w}$ is the disturbance. The parameters Δf, Δg_1, and Δg_2 are uncertain smooth vector fields and mappings. $\delta J = J^{-1} \Delta J J^{-1}$. For small perturbations, f, g_1, g_2, h_1, Δf, Δg_1, and Δg_2 can be expressed as

$$f(\pmb{x}) = \begin{bmatrix} -J^{-1} \mathrm{q}^\times J \mathrm{q} \\ Q(\pmb{q}) \pmb{\omega} \end{bmatrix}, g_1(\pmb{x}) = \begin{bmatrix} J^{-1} \\ 0 \end{bmatrix}, g_2(\pmb{x}) = \begin{bmatrix} J^{-1} B \\ 0 \end{bmatrix}$$

$$h_1(\pmb{x}) = \sqrt{\rho_1 \mathrm{q}^T J \mathrm{q} + \rho_2 \eta^2(q_0)}$$

$$\Delta f(\pmb{x}) = \begin{bmatrix} -J^{-1} \mathrm{q}^\times J \mathrm{q} + J^{-1} \delta J \mathrm{q}^\times J \mathrm{q} + J^{-1} \delta J \mathrm{q}^\times \Delta J \mathrm{q} \\ 0 \end{bmatrix}$$

$$\Delta g_1(\pmb{x}) = \begin{bmatrix} -\delta J \\ 0 \end{bmatrix}, \Delta g_2(\pmb{x}) = \begin{bmatrix} J^{-1} \Delta B - \delta J(B + \Delta B) \\ 0 \end{bmatrix}, \text{etc.}$$

1. Robust Nonlinear State Feedback Theory

Consider a nonlinear state-space system G_0 with

$$\dot{\underline{x}} = f(\underline{x}) + g(\underline{x}) \underline{w} \tag{17a}$$

$$z = h(\pmb{x}) \tag{17b}$$

where $\underline{x}$ is the state vector, $\underline{w}$ is the exogenous disturbance to be rejected, and $\underline{z}$ is the penalized output signal. We assume that $f(\underline{x})$, $g(\underline{x})$, and $h(\underline{x})$ are C^∞ functions and $\underline{x} = 0$ is the equilibrium point of the system, that is, $f(0) = h(0) = 0$.

Given a positive number $\gamma > 0$, the system in Eq. (17) has a finite $L_2 -$ gain less than γ for all $\underline{w} \in L_2[0,T]$ with $0 \le T < \infty$,

$$\int_0^T \left\| \underline{z}(t) \right\|^2 dt \le \gamma^2 \int_0^T \left\| \underline{w}(t) \right\|^2 dt. \tag{18}$$

Lemma 1 Assume that $\Delta f(\underline{x}) = 0$, $\Delta g_1(x) = 0$, and $\Delta g_2(\underline{x}) = 0$ in Eq. (16). If $(f(\underline{x}), h_1(\underline{x}))$ is zero-detectable and a positive definite function $V(\underline{x})$ exists so that the Hamilton–Jacobi partial differential inequality

$$H_\gamma = V_{\underline{x}}^T f + \frac{1}{2} V_{\underline{x}}^T \left(\frac{1}{\gamma^2} g_1 g_1^T - g_2 g_2^T \right) V_{\underline{x}} + \frac{1}{2} h_1^T h_1 < 0 \tag{19}$$

holds [2, 9, 12], then the system has a finite L_2 gain less than γ. Once $V(\underline{x})$ is obtained, the control signal $\underline{u}$ can be synthesized as

$$\underline{u} = -g_2^T V_{\underline{x}} \tag{20}$$

where

$$V_{\underline{x}} = \begin{bmatrix} \dfrac{\partial V}{\partial x_1} & \dfrac{\partial V}{\partial x_2} & \cdots & \dfrac{\partial V}{\partial x_n} \end{bmatrix}^T.$$

Theorem 1 Consider the nonlinear uncertain system in Eq. (16) and that the system parameters satisfy the following equation [7, 8]:

$$\Delta f(\underline{x}) = \Phi(\underline{x}) \Psi^T(\underline{x}), \Delta g_1(\underline{x}) \Delta g_1^T(\underline{x}) \le G_1(\underline{x}) G_1^T(\underline{x}),$$

and

$$\Delta g_2(\underline{x}) \Delta g_2^T(\underline{x}) \le G_2(\underline{x}) G_2^T(\underline{x}),$$

where $\Phi(\underline{x}) \in \mathbb{R}^{n \times m}$, $\Psi(\underline{x}) \in \mathbb{R}^{1 \times m}$, and $G_i(\underline{x}) \in \mathbb{R}^{n \times p_i}$, $i = 1, 2$, are known vectors. For these vectors, we assume that there exist scale functions $\Theta(\underline{x}) \ge 0$ with $\Psi(\underline{x})$ described by $\left\| \Psi(\underline{x}) \right\| \le \Theta(\underline{x})$, where $\Theta(0) = 0$. Under this assumption, Eq. (16) satisfies the following conditions:

(i) $(f(\underline{x}) + \Delta f(\underline{x}), h_1(\underline{x}))$ is zero-state detectable.

(ii) there exists a smooth function $\sigma = \sigma(\underline{x}) > 0$ so that the following Hamilton–Jacobi partial differential inequality holds:

$$V_{\underline{x}}^T f + \frac{1}{2} V_{\underline{x}}^T \left(\frac{1}{\gamma^2} (1 + \sigma) g_1 g_1^T - (1 - \sigma) g_2 g_2^T \right) V_{\underline{x}}$$

$$+ \frac{1}{2} V_{\underline{x}}^T \left(\frac{1}{\gamma^2} \frac{1 + \sigma}{\sigma} G_1 G_1^T + \frac{1 - \sigma}{\sigma} G_2 G_2^T + \sigma \Phi \Phi^T \right) V_{\underline{x}}$$

$$+ \frac{1}{2\sigma} \Psi^T \Psi + \frac{1}{2} h_1^T h_1 \le 0 \tag{21}$$

This inequality has a smooth positive solution $V(\underline{x})$, where $x \in X$, and X is a neighborhood of the origin in $\mathbb{R}^n$. Then, the state feedback law

$$u(\underline{x}) = -g_2^T V_{\underline{x}} \tag{22}$$

ensures that the system in Eq. (16) has a robust performance.

V. EXTENDED KALMAN FILTER

For enhancing the accuracy and performance of the filter, a UKF algorithm was used in the satellite attitude determination process [1, 4]. The normal method involves the use of the extended Kalman filter (EKF), which leads to the following

problems: 1) the higher-order terms in the Taylor expansion of a nonlinear function cannot be neglected, and 2) linearization causes major errors in the system, even rendering the filter unstable in the iterative process. Moreover, the Jacobian matrix derivation of a nonlinear function is difficult with numerous problems.

The state equation and the measurement equation of the EKF have the following standard forms:

$$x_{k+1} = f(x_k, u_k, w_k) \tag{23a}$$

$$z_k = h(x_k, v_k) \tag{23b}$$

where x_k is the n-dimensional state vector of the system; P_k, the variance; u_k the r-dimensional input vector; f the n-dimensional vector function; h, the m-dimensional vector function; w_k, the p-dimensional stochastic process noise; Q, the variance matrix; v_k, q-dimensional random noise; and R, the variance matrix.

The difference between the UKF and the EKF is that the UKF uses sampling point conversion to calculate the state and measure the average and variance of forecast values. In the sampling point conversion process, the average value and variance of estimates are used to generate a group of discrete sampling points, and these points are spread using the state equation and measurement output equation. The average value and variance of the forecast values are then generated through weighted summation. The generation of sampling points is as follows:

The augmented state variable is $\hat{x} = \left[x_k^T, w_k^T, v_k^T \right]^T$.

1) Select ε sampling points

$$\chi_{0,k} = \hat{x}_k \tag{24a}$$

$$\chi_{i,k} = \hat{x}_k + \left(\sqrt{(n+\varepsilon_0) P_k} \right)_i^T, \quad i = 1, 2, \cdots, n \tag{24b}$$

$$\chi_{i+n,k} = \hat{x}_k - \left(\sqrt{(n+\varepsilon_0) P_k} \right)_i^T, \quad i = 1, 2, \cdots, n \tag{24c}$$

2) Calculate weights

$$W_0^m = \frac{\varepsilon_0}{(n+\varepsilon_0)} \tag{25a}$$

$$W_0^c = W_0^m + \left(1 - \varepsilon_1^2 + \varepsilon_2\right) \tag{25b}$$

$$W_i^m = W_i^c = \frac{1}{2(n+\varepsilon_0)}, \quad i = 1, 2, \cdots, n \tag{25c}$$

where $\varepsilon_0 = \varepsilon_1^2 (n+\kappa) - n$; ε_1 and κ are undetermined parameters.
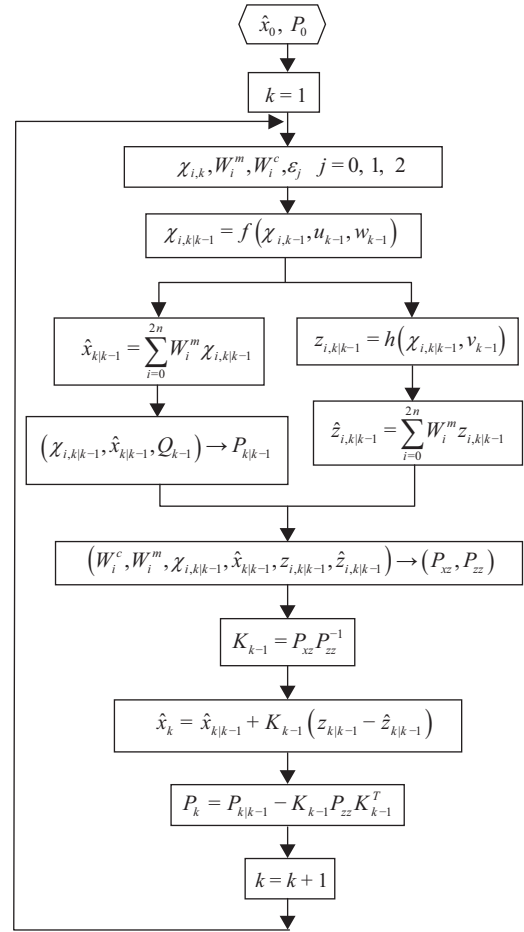
Fig. 3. Flow chart of the extended Kalman filter algorithm.

The parameter ε_1 is set as a small positive number (*e.g.*, $10^{-4} \le \varepsilon_1 \le 1$), and it determines the range of sampling points circling $\hat{x}$. The influence of the higher-order terms of the nonlinear equation can be reduced by controlling ε_1. The accuracy of the variance can be increased by controlling ε_2. The optimal ε_2 is 2 for a Gaussian distribution. The parameter κ is a scale factor that has a value of 2 when the system is invariable. Let $\kappa = 3 - n$ if κ is a multivariable. The term $\left(\sqrt{(n+\varepsilon_0) P_k} \right)_i$ represents the ith row of a matrix root. The flow chart of the extended Kalman filter algorithm is shown in Fig. 3.

VI. MEASUREMENT REFERENCE MODEL

1. Geomagnetic Field Model

The International Geomagnetic Reference Field (IGRF) model [5] was used in this study as the mathematical simulation model of the geomagnetic field of a gyroless satellite. In Eq. (26), r is the distance between the satellite and the earth's center in the ECEF coordinate system, λ is the longitude of the satellite in the ECEF coordinate system, ϑ is the colatitude of the satellite in the ECEF coordinate system (90° minus

latitude), $R_\oplus$ is the semimajor axis of the earth (6371.2 km), g and h are the Gaussian coefficients of the IGRF model, P_n^m is the Legendre function with $m \le n$. Because the Gaussian coefficients g_n^m and h_n^m used in the IGRF model are derived from measured geomagnetic field values through least square matching, the Gaussian coefficients should be remeasured and updated approximately every 5 years [5, 13]. The order number of the Gaussian coefficients of the IGRF model is 10. Therefore, n in Eq. (26) can be 1 to ∞ and m ranges from 0 to n.

$$V(r, \lambda, \vartheta) = R_\oplus \bullet$$

$$\sum_{n=1}^{\infty} \sum_{m=0}^{n} \left(\frac{R_\oplus}{r}\right)^{n+1} \left(g_n^m \cos(m\lambda) + h_n^m \sin(m\lambda)\right) P_n^m(\vartheta) \qquad (26)$$

The geomagnetic field vector $\boldsymbol{B}_g$ can be derived from the negative gradient of the geomagnetic field potential function V in Eq. (26):

$$\boldsymbol{B}_g = -\nabla V \qquad (27)$$

The relational expression of geomagnetic field vector $\boldsymbol{B}_g$ and satellite position, i.e. the component of magnetic field V in the north, east and earth directions in the geographic coordinate system. The relationship between the geomagnetic field vector and the satellite position can be obtained as

$$\boldsymbol{B}_g = \begin{bmatrix} B_x & B_y & B_z \end{bmatrix}^T = \left[\frac{1}{r}\frac{\partial V}{\partial \vartheta} \quad -\frac{1}{r\sin\vartheta}\frac{\partial V}{\partial \lambda} \quad \frac{\partial V}{\partial r} \right]^T \qquad (28)$$

The IGRF describes the geomagnetic field intensity in the ECEF coordinate system, the relation of geomagnetic field vector $\boldsymbol{B}_g$ in the spherical coordinates of geomagnetic field and the ECI coordinate system i shows as long as the north, east and earth geomagnetic coordinates circle around oY_λ axis by $(180 - \vartheta)$ in turn, and circle around oY_ϑ by $-\alpha$, the ECI coordinate system is obtained. The transition matrix C_g^i for transformation from the geographic coordinate system to the ECI coordinate system is

$$C_g^i = C_x(-\alpha) C_y(180 - \vartheta), \; \boldsymbol{B}_i = C_g^i \boldsymbol{B}_g \qquad (29)$$

In Eq. (29), $\alpha = (\lambda + G)$ is the right ascension, and G is the Greenwich right ascension of the meridian or GST.

For simulation analysis, the IGRF model was used to simulate the real geomagnetic field. The tenth-order spherical order number was selected for the simulation, ensuring sufficiently high geomagnetic field accuracy. It is determined according to the performance of the magnetometer and the attitude determination accuracy in the simulation. To confirm whether the aforementioned result is correct, the magnetic
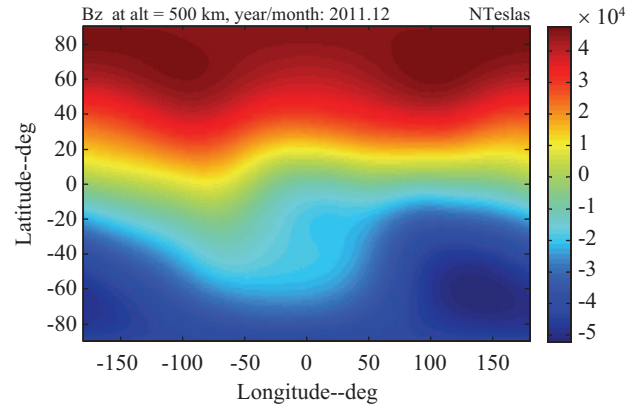
Fig. 4. Magnetic field distribution at the altitude of a microsatellite in orbital coordinates.

field intensity of tenth-order IGRF in the orbit system is shown in Fig. 4.

2. Magnetometer Model

Three magnetometers were fixed for obtaining measurements of the local magnetic field intensity along the three axes of the body coordinate system. A three-axis magnetometer was fixed parallel to the satellite body axis to measure the body yaw angle. Assume $\boldsymbol{B}_g = \begin{bmatrix} B_x & B_y & B_z \end{bmatrix}^T$ to be the geographic coordinates of the geomagnetic field. Further, let C_g^i and C_i^o be the transition matrix for the conversion of the geographic coordinate system into the ECI coordinate system and the transition matrix for conversion from the ECI coordinate system to the orbital coordinate system, respectively. The component of the geomagnetic field vector in the orbit system can be expressed as

$$\boldsymbol{B}_o = C_i^o C_g^i \boldsymbol{B}_g \qquad (30)$$

The component of the geomagnetic field in the satellite body system can be obtained from measured and estimated magnetic field values:

$$\boldsymbol{B}_b = C_o^b C_i^o C_g^i \boldsymbol{B}_g + \upsilon_b \qquad (31)$$

where υ_b is the zero-mean white noise, that is,

$$\upsilon_b \sim \left(0, \sigma_g^2\right) \qquad (32)$$

3. Sun Vector Model

The satellite attitude was estimated from the vector observations obtained from the sun sensor. The method presented in [6] was used in this study, and a sun model was constructed on the basis of the relationship between the earth and the sun. Because the angle between sunrays and the equatorial plane of
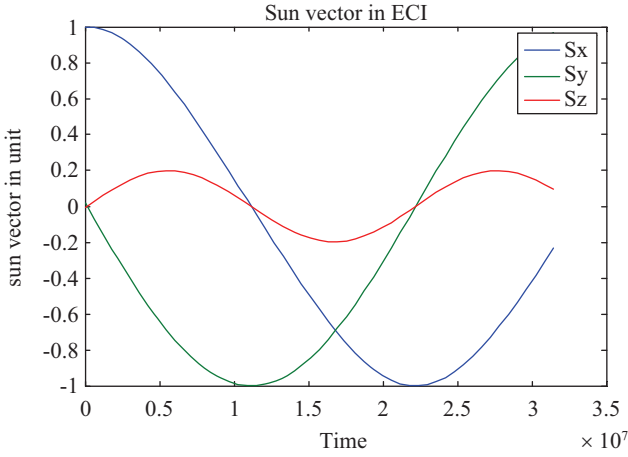
Fig. 5. Sun vector in the inertial system within one year from vernal equinox.

Fig. 6. CSS reading error of 5% for a FOV of 70°.

the earth changes periodically within the Tropics of Capricorn and Cancer (±23°) during the course of a year, the elevation of sunrays in the ECI coordinate system is

$$\varepsilon_s = \frac{23\pi}{180}\sin\left(\frac{2\pi T_\Psi}{365}\right) \tag{33}$$

where T_Ψ is the time elapsed since vernal equinox. The sun azimuth for a period of a year starting from vernal equinox can be given as

$$\lambda_s = \frac{2\pi T_\Psi}{365} \tag{34}$$

when the earth passes by the vernal equinox, the unit vector in the direction of sunrays in the ECI coordinate system is

$$s_0^{\varpi_i} = \begin{bmatrix} 1 & 0 & 0 \end{bmatrix}^T.$$

Then, the sun vector at any time is

$$s^{\varpi_i} = C_y(\varepsilon_s)C_z(\lambda_s)s_0^{\varpi_i}, \; s^{\varpi_o} = C_i^o s^{\varpi_i},$$

$$C_i^o = C_z(\omega + v)C_x(i)C_z(\Omega) \tag{35}$$

where s^{ϖ_i} is the sun vector in the ECI coordinate system, s^{ϖ_o} is the sun vector in the orbit system, C_i^o is the transition matrix for converting the ECI coordinate system into the orbit system. According to the sun model, the sun vectors in the ECI and orbit coordinate systems within one year from the vernal equinox are shown in Fig. 5.

4. CSS Reading Algorithm

CSS Reading Algorithm (sun vector Computation by CSS Reading Algorithm)

1) CSS Geometric Configuration and Sun Vector

If the microsatellite uses eight CSSs to calculate the sun vector, on the basis of the present orientation configuration and field-of-view (FOV) values of the CSS, there will be at most four CSSs irradiated by the sun, and this number may decrease to three and two CSSs. Thus, the algorithm varies in the three cases of different numbers of CSSs irradiated by the sun.

Let the real sun vector be

$$\boldsymbol{S}_{real} = \begin{bmatrix} S_{real\_x} & S_{real\_y} & S_{real\_z} \end{bmatrix}^T \tag{36}$$

The relationship between the current generated by the eight CSSs and the sun vector is

$$\boldsymbol{I}_i = \boldsymbol{I}_0 \boldsymbol{N} \boldsymbol{S}_{real}$$

$$\boldsymbol{I}_{norm} = \boldsymbol{I}_i / \boldsymbol{I}_0 = \boldsymbol{N} \boldsymbol{S}_{real} \tag{37}$$

where $\boldsymbol{I}_i = \begin{bmatrix} I_1 & I_2 & \cdots & I_8 \end{bmatrix}^T$ is the current generated by the various CSSs when irradiated by the sun; $\boldsymbol{I}_0$, the maximum current output of the CSSs (for FORMOSAT-3, $\boldsymbol{I}_0 = 167$ mA); and $\boldsymbol{N}$, the normal vector orientation of the eight CSSs.

$$\boldsymbol{N}^T = \begin{bmatrix} N_1 & N_2 & N_3 & N_4 & N_5 & N_6 & N_7 & N_8 \end{bmatrix}$$

$$= \begin{bmatrix} a_1 & a_2 & a_3 & a_4 & a_5 & a_6 & a_7 & a_8 \\ b_1 & b_2 & b_3 & b_4 & b_5 & b_6 & b_7 & b_8 \\ c_1 & c_2 & c_3 & c_4 & c_5 & c_6 & c_7 & c_8 \end{bmatrix} \tag{38}$$

2) Cases of Four, Three, and Two CSSs Irradiated by the Sun

There were 2000 data samples for the regime analysis of a 5% reading error of the CSSs (in relation to reading) and 70° FOV of the CSSs, as shown in Fig. 6. (Note: The read noise of a sensor is the noise for a normal Gaussian distribution.)
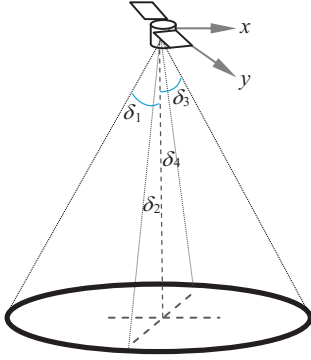
Fig. 7. Attitude measurement by the static horizon sensor.

5. Earth Horizon Sensor Model

The static infrared horizon sensor is also known as radiant heat balance earth sensor. The static horizon sensor is fixed to the side of the satellite facing the earth, and it consists of 14-16 μm filter lenses and four thermopile detectors. The angles between the spectral axes of the four detectors and the principal optic axis can be set according to the distance of the satellite from the earth, and it is set to ensure that the center of the earth disc is in the FOV of the four detectors, as shown in Fig. 7. When the satellite attitude shows a deviation, the output of the four probes will change accordingly. Then,

$$\varphi = \frac{\delta_2 - \delta_4}{2} \tag{39a}$$

$$\theta = \frac{\delta_1 - \delta_3}{2} \tag{39b}$$

where φ is the roll attitude angle of the satellite and θ is the pitch attitude angle.

VII. ATTITUDE DETERMINATION AND SUBSYSTEM ANALYSIS

1. CSS + Scanning Horizon Sensor + Three-Axis Magnetometer Satellite Attitude Estimation

1) Attitude Estimation State Variable

The nine-dimensional attitude estimation state variable was used for the microsatellite:

$$\hat{x} = \left[\hat{\dot{\phi}} \quad \hat{\dot{\theta}} \quad \hat{\dot{\psi}} \quad \hat{\phi} \quad \hat{\theta} \quad \hat{\psi} \quad \int\hat{\phi} \quad \int\hat{\theta} \quad \int\hat{\psi} \right]^T \tag{40}$$

2) Direct Observation Equation

If the attitude is measured using the CSS, horizon sensor, and magnetometer instead of a gyro, the measurement outputs of these instruments are directly considered as the observations. The filter output value should be compared with the observed

value, and therefore, the most straightforward observation vector can be chosen as the measured value of the sun vector S_b, horizon sensor E_b, and three-dimensional geomagnetic field vector B_b in the satellite body system, that is,

$$z = \begin{bmatrix} S_b^T & E_b^T & B_b^T \end{bmatrix}^T$$

$$= \begin{bmatrix} S_{bx} & S_{by} & S_{bz} & | & E_{bx} & E_{by} & E_{bz} & | & B_{bx} & B_{by} & B_{bz} \end{bmatrix}^T \tag{41}$$

The corresponding measure equation is

$$z = h(x) + v = \begin{bmatrix} C_o^b(x)S_o \\ C_o^b(x)E_o \\ C_o^b(x)B_o \end{bmatrix} \tag{42}$$

where $v = \begin{bmatrix} v_S^T & v_E^T & v_B^T \end{bmatrix}^T$ is the measurement noise of the CSS, horizon sensor, and magnetometer. S_o, E_o, and B_o are the sun vector, earth radiation vector, and geomagnetic field vector, respectively, determined from the orbital location look-up table of the microsatellite.

3) Simulation Results and Analysis

The gyroless EKF designed was simulated. As the satellite experiences large-angle attitude motion and attitude stabilization motion in the attitude capture process, its attitude changes frequently. Therefore, the attitude changes in the satellite attitude capture process are used for attitude filter estimation, from the filtered values of the measurements of the CSS + scanning horizon sensor + three-axis magnetometer on a gyroless EKF.

4) Simulated Conditions

The magnetometer measurement error was 500 nT, the solar sensor measurement error was 10%, and the three-axis initial attitude of the microsatellite was different.

5) EKF Initial Attitude

The satellite mission orbit information was as follows: satellite altitude, 500 km; longitude, 108°; latitude, 35°; and sampling time, 4 s; and off-modulator magnitude, 2. The satellite attitude motion trajectory is shown in Fig. 8. The CSS tasks decreased from four to two at 200 s, and the CSS did not work when the satellite entered the earth's shadow area at 600 s. The EKF involving a direct observation equation was used in the simulation.

In Fig. 8(a), the estimated time response of the microsatellite body rate is shown along with the difference between the measured and the estimated body rates when the number of CSSs was reduced from four to two at 200 s and from two to zero at 600 s. In Fig. 8(b), the time response of the estimated microsatellite Euler angle is shown with the difference between the measured and estimated values of the angle when
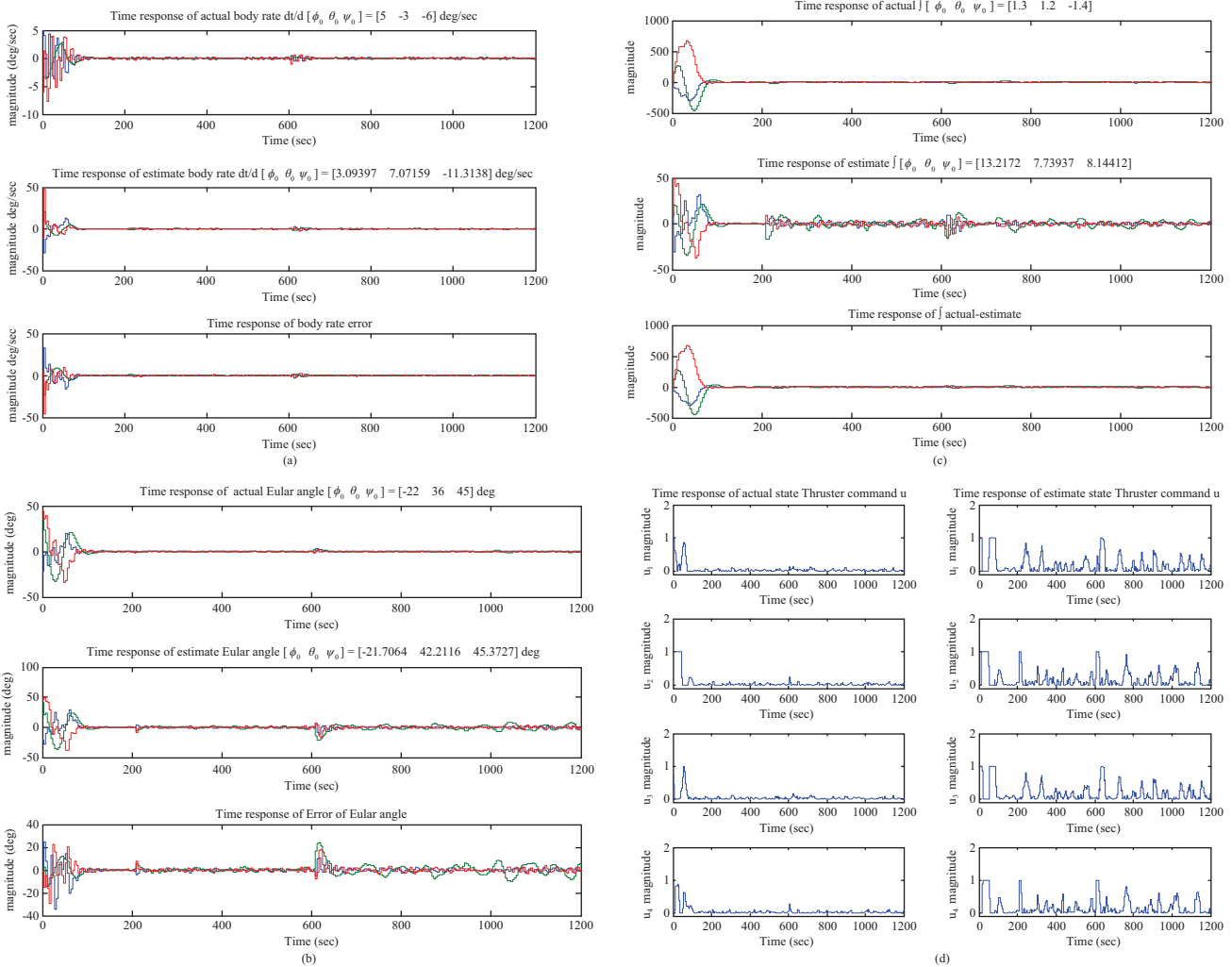
Fig. 8. Time response of satellite body rate, Euler angle and angular integration.

the number of CSSs was reduced from four to two at 200 s and from two to zero at 600 s. The time response of estimated angular integration is shown in Fig. 8(c); the estimated values and the difference between the measured and estimated values when the number of CSSs was reduced from four to two at 200 s and from two to zero at 600 s are also shown. Finally, the time response of the microsatellite thrusters actual and estimated command of *u* for the two instances of a decrease in the number of CSSs are shown in Fig. 8(d).

VIII. CONCLUSION

The simulation results show that when the combination of the CSS, scanning horizon sensor, and three-axis magnetometer functions normally, the estimation of a large-angle attitude change has a relatively small error. The maximum error is 10°. When the number of CSSs is reduced, the error is relatively large. When the attitude changes, the maximum instantaneous error is 32°. In the academic theory and engineering practice, on the whole, a systematic analysis is feasible.

REFERENCES

1. Crassidis, J. L. and Markley, F. L., "Unscented filtering for spacecraft attitude estimation," *Journal of Guidance, Control, and Dynamics*, Vol. 26, pp. 536-542 (2003).
2. Isidori, A. and Astolfi, A., "Disturbance attenuation and H_∞-control via measurement feedback in nonlinear systems," *IEEE Transaction on Automatic Control*, Vol. 37, No. 9, pp. 1283-1293 (1992).
3. Julier, S. J., Uhlmann, J. K., and Durrant-Whyte, H. F., "A new approach for filtering nonlinear systems," *American Control Conference*, Vol. 3, pp. 1628-1632 (1995).
4. Lefferts, E. J., Markley, F. L., and Shuster, M. D., "Kalman filtering for spacecraft attitude estimation," *Journal of Guidance, Control, and Dynamics*, Vol. 5, pp. 417-429 (1982).
5. Psiaki, M. L., Huang, L., and Fox, S. M., "Ground tests of magnetometer-based autonomous navigation (MAGNAV) for low-earth-orbiting space-

craft," *Journal of Guidance, Control, and Dynamics*, Vol. 16, pp. 206-214 (1993).

6. Sedlund, C. A., "A simple sun-pointing magnetic controller for satellites in equatorial orbits," *IEEE Aerospace Conference*, pp. 1-12 (2009).

7. Shou, H. N. and Lin, C. T., "Micro-satellite detumbling mode attitude determination and control: UKF approach," *Storage Management Solutions*, Vol. 5, pp. 35-41 (2011).

8. Shou, H. N. and Lin, C. T., "Micro-satellite attitude determination: Using Kalman filtering of magnetometer data approach," *Journal of Industrial Technology*, Vol. 28, No. 4, pp. 173-180 (2012).

9. Sidi, M. J., *Spacecraft Dynamics and Control: A Practical Engineering Approach*, Cambridge University Press (1997).

10. Stoltz, P. M., Sivapiragasam, S., and Anthony, T., "satellite orbit-raising using LQR control with fixed thrusters," *Advances in Astronautical Science*, AAS 98-007, pp. 1-13 (1998).

11. Vallado, D. A. and McClain, W. D., *Fundamental of Astrodynamics and Applications*, Second Edition, Microcosm Press (2001).

12. van der Schaft, A. J., "L_2-gain analysis of nonlinear systems and nonlinear state-feedback H_∞ control," *IEEE Transaction on Automatic Control*, Vol. 37, No. 6, pp. 770-784 (1992).

13. Wertz, J. R., Everett, D. F., and Puschell, J. J., *Space Mission Engineering: The New SMAD*, Microcosm Press (2011).